

# Temporal shaping and time varying orbital angular momentum of displaced vortices.

FAZELE HOSSEINI<sup>1</sup>, MOHAMMAD A. SADEGHZADEH<sup>1,\*</sup>, AMIR RAHMANI<sup>1,2</sup>,  
FABRICE P. LAUSSY<sup>3,4</sup>, AND LORENZO DOMINICI<sup>5</sup>

<sup>1</sup>Department of Physics, Yazd University, Yazd, Iran

<sup>2</sup>Department of Physics, Azarbaijan Shahid Madani University, Tabriz, Iran

<sup>3</sup>Faculty of Science and Engineering, University of Wolverhampton, Wulfruna St, Wolverhampton WV1 1LY, UK

<sup>4</sup>Russian Quantum Center, Novaya 100, 143025 Skolkovo, Moscow Region, Russia

<sup>5</sup>CNR NANOTEC, Istituto di Nanotecnologia, Via Monteroni, 73100 Lecce, Italy

\*msadeghzadeh@yazd.ac.ir

Compiled August 28, 2020

The fundamental mode of rotation in quantum fluids is given by a vortex, whose quantized value yields the orbital angular momentum (OAM) per particle. If the vortex is displaced (off-centered) from the reference point for rotation, the angular momentum is reduced and becomes fractional. Such displaced vortices can further exhibit a peculiar dynamics in presence of confining potentials or couplings to other fields. We study analytically a number of 2D systems where displaced vortices exhibit a noteworthy dynamics, including time-varying self-sustained oscillation of the OAM, complex reshaping of their morphology with possible creation of vortex-antivortex pairs and peculiar trajectories for the vortex core with sequences of strong accelerations and decelerations which can even send the core to infinity and bring it back. Interestingly, these do not have to occur conjointly, with complex time dynamics of the vortex core and/or their wavepacket morphology possibly taking place without affecting the total OAM. Our results generalize to simple and fundamental systems a phenomenology recently reported with Rabi-coupled bosonic fields, showing their wider relevance and opening prospects for new types of control and structuring of the angular momentum of light and/or quantum fluids. © 2020 Optical Society of America under the terms of the [OSA Open Access Publishing Agreement](#)

<http://dx.doi.org/10.1364/optica.XX.XXXXXX>

## 1. INTRODUCTION

Topology is essential to different areas of physics, in particular to condensed matter physics [1, 2]. This involves invariants under deformation from the ground state to a new configuration for which any path to the ground state is energetically too costly. As such, topological invariants powered by Homotopy groups provide subtle tools to detect holes in a given space. Examples are topological defects in systems with continuous broken symmetry. A vortex is a typical such defect in systems with global  $U(1)$  broken symmetry. It is characterized by a null density region and an integer (topological) charge associated to a singularity in the gradient of the phase of the order parameter, which defines the core of the vortex. In this way, the topological charge (TC)

defines an intrinsic orbital angular momentum (OAM) embedded in the vortex state. Vortices are common in many media and systems, including light [3, 4] and quantum matter, such as superconductors [5], superfluids [6] or atomic Bose Einstein condensates [7], among others. Vortices also recently flourished in coupled light-matter, so-called “polaritons”, systems [8–14] that can interpolate between the purely optical and strongly interacting condensed matter cases.

A vortex beam (VB)—a vortex confined in a beam with a spiral wavefront—is special as it can carry angular momentum [15], which can further be distinguished between one of two kinds: either with a non-uniform phase-varying wavefront, which is called an “anisotropic VB”, or with a uniform phase variation,

which is referred to as an “isotropic VB”. In both cases, an interesting situation arises when the core of the vortex is displaced from the center of the beam, a situation which does not arise in infinite-size systems. This leads to a reduced angular momentum, which is still fixed, and to a modified morphology for the phase of the field (its distribution in space [15]). For a static VB (not varying in time), either isotropic or anisotropic, it is known that the vortex angular momentum can be described by a combination of elementary vortices with integer topological charges, which determines the overall morphology and associated angular momentum across the beam [16].

Vortex beams can also be dynamic, i.e., their angular momentum can be time dependent. It is only recently, however, that VB have entered this regime [17, 18]. The earliest report, to the best of our knowledge, was by some of the present authors and collaborators [17] in the highly versatile polaritonic platform [19]. There, a time-varying angular momentum was shown to be self-sustained by the interplay between Rabi oscillations and VB morphologies in two coupled fields. This was achieved by preparing the system in a special topological initial condition imprinted in the microcavity polariton field with two delayed pulses of different topological charge. This produced a rich temporally and spatially structured dynamics of the off-centered core in the polariton fluid resulting in oscillating linear and angular momenta of the emitted light. Such oscillations happen in the linear regime and can be described exactly. We study further this case in the last Section of the present text. A similar scheme, with two retarded pulses but now partially overlapping in time, has also been used in the nonlinear process of high harmonic generation, resulting in a vortex beam with continuously time-varying angular momentum [18].

Here, we study analytically fundamental and simple physical systems that display similar nontrivial motion of a dynamical vortex. The results are quite remarkable given the complex and far-reaching phenomenology that is displayed by a simple theoretical model, which basically reduces to a first-year quantum mechanics textbook exposition. Given the ease of access of both the experimental scheme (combinations of pulsed excitations with various TC) and the variety of possible platforms where to explore such Physics, we expect the field of dynamic VB to quickly take off in a variety of systems in the near future. What we find is that such displaced vortices sustain a rich dynamics with a morphology that is stretched or folded up in time to accompany the variation of the angular momentum. Interestingly, although one may expect a time-varying morphology to also result in a time-varying angular momentum, we show that this is not compulsorily the case. To this end, we consider a displaced vortex in several elementary systems, namely, an infinite (circular) quantum well potential (Section 2), a slightly anharmonic potential (Section 3), a spatially squeezed harmonic potential (Section 4) and the already discussed case of two coupled condensates (polaritons, in Section 5). Section 6 concludes and gives general remarks. It is worth noting that all the examples considered hereon are in the linear regime, where the self-interaction between particles is negligible. The phenomenology is however robust in the sense that it is maintained in the presence of nonlinearities or interactions, as we have checked numerically. In such cases, however, further complications arise with more complex reshaping of the vortices, proliferations of vortex-antivortex pairs and other features which we leave for other studies.

## 2. INFINITE CIRCULAR QUANTUM WELL

Our first platform to consider the dynamics of a displaced-vortex in a VB is the fully-confined case with the canonical circular geometry, namely, the infinite circular quantum well. This provides an example of interactions between vortices and the system’s boundaries. As we show below, interference between the rotating wavepacket and its reflection from the hard walls leads to a time-dependent morphology of the phase, which, nevertheless, leaves the expectation value for the total angular momentum invariant, as expected from the conservation rules. Manipulating the size of the initial packet introduces different content of radial momentum adding up to the rotational one. This leads to various regimes for the dynamics, ranging from a smooth rotation of the pattern to pair-creation of vortices/antivortices. Such a case can be realized experimentally for instance with polaritons in etched micropillars [20–22]. The Hamiltonian for a circular quantum well of radius  $R$  reads as

$$H_{qw} = -\frac{\hbar^2}{2m}\nabla^2 + V(r), \quad (1)$$

with

$$V(r) = \begin{cases} 0 & r < R \\ \infty & r > R \end{cases}, \quad (2)$$

where  $r = \sqrt{x^2 + y^2}$  and  $\varphi = \arg(x + iy)$ . The system is easily integrated exactly. Solving the equation  $H_{qw}\chi_{n,l} = E_{n,l}\chi_{n,l}$ , one finds the eigenstates and eigenenergies as

$$\chi_{n,l} = \frac{N_{n,l}}{\sqrt{2\pi}} e^{il\varphi} J_{|l|}(k_{n,l}r), \quad (3a)$$

$$E_{n,l} = \frac{\hbar^2 k_{n,l}^2}{2m} = \frac{\hbar^2}{2mR^2} \beta_{n,l}^2, \quad (3b)$$

where  $J_{|l|}$  is the Bessel function of integer order,  $N_{n,l}$  is the normalization constant,  $l = 0, \pm 1, \pm 2, \dots$ , and  $\beta_{n,l} = k_{n,l}R$  is the  $n$ th zero of the  $|l|$ th Bessel function for which  $J_{|l|}(\beta_{n,l}) = 0$  as imposed by the boundary condition, namely  $\chi_{n,l}(R, \varphi) = 0$ . From these stationary solutions  $\chi_{n,l}$ , one then solves Schrödinger’s equation  $i\hbar\partial_t\psi = H\psi$  for any initial state  $\psi_0(r, \varphi) \equiv \psi(r, \varphi, 0)$  as the linear superposition

$$\psi(r, \varphi, t) = \sum_{n,l} \alpha_{n,l} e^{-iE_{n,l}t/\hbar} \chi_{n,l}(r, \varphi), \quad (4a)$$

$$\alpha_{n,l} = \int d\varphi \int r dr \psi_0 \chi_{n,l}^*(r, \varphi). \quad (4b)$$

To describe the dynamics of a displaced vortex, we take for the initial condition a superposition of two Bessel–Gauss wavepackets, one with topological charge  $TC = 1$  and another with  $TC = 0$ :

$$\psi_0 = \begin{cases} e^{-r^2/2w^2} (J_1(k_{1,1}r)e^{i\varphi} + a_c J_0(k_{1,0}r)) & r < R \\ 0 & r > R \end{cases}, \quad (5)$$

where  $w$  is the spot size of the wavepacket and  $a_c$  is a free parameter that upon tuning the relative strength between the two wavepackets controls the offset position of the vortex core. The wavepacket solution in time is then given by

$$\psi(r, \varphi, t) = \sum_n \left[ \alpha_{n,1} e^{-iE_{n,1}t/\hbar} \chi_{n,1} + \alpha_{n,0} e^{-iE_{n,0}t/\hbar} \chi_{n,0} \right]. \quad (6)$$

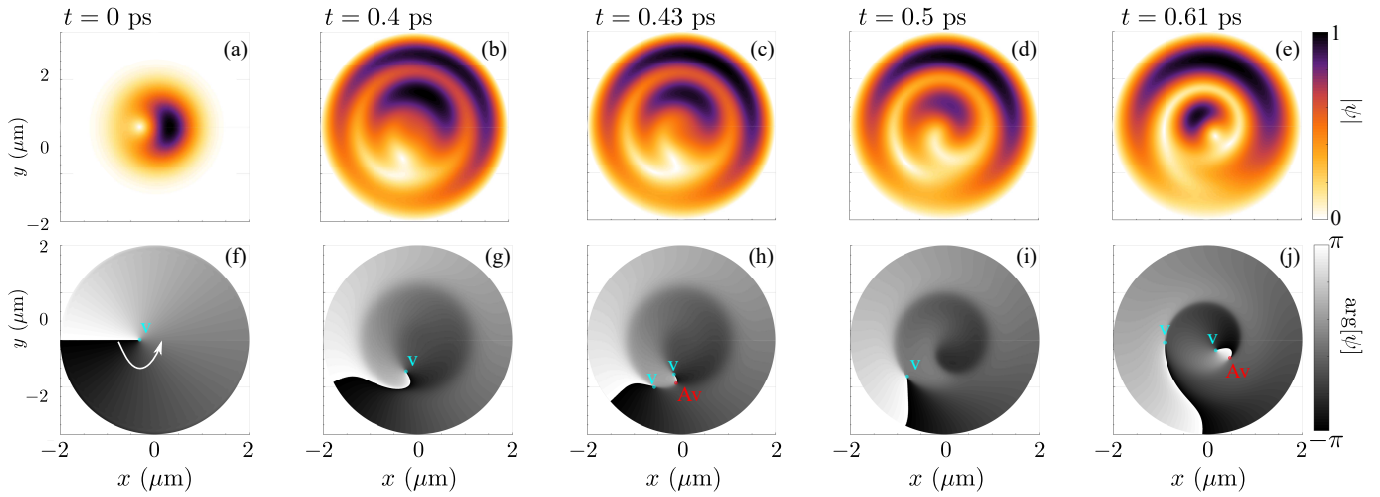


**Fig. 1.** Dynamics of an off-centered (displaced) vortex in an infinite circular quantum well, in the regime  $w \ll R$ . The upper panels show the density profile  $|\psi|$  of the wavepacket at different times. The lower panels illustrate the corresponding phase map  $\arg[\psi]$ . In (h), the phase gets so distorted that a pair is excited, shown by V (vortex) and AV (antivortex). The pair moves until V and AV recombine. It gets excited again later, as shown in (j). Parameters:  $R = 2 \mu\text{m}$ ,  $w = 0.5 \mu\text{m}$ , and  $a_c = 0.3$ .

The dynamics strongly depends on the size  $w$  of the packet. When  $w$  is of the order of quantum well size  $R$ , the terms in Eq. (6) that dominate are those weighted by  $\alpha_{1,1}$  and  $\alpha_{1,0}$ , which results in a smooth rotation of the wave packet, with simply a quantum beating between two states. However, when  $w$  is smaller than  $R$  by one order of magnitude or more, a larger number  $\alpha_{n,i}$  ( $i = 0, 1$ ) enter the dynamics, which acquires a markedly different character as higher  $n$  amplitudes become significant. Examples are shown in Fig. 1. We can observe different stages in the dynamics. At first, we see an increase of the wavepacket size inside the well as a result of its diffusion, which also separates the minima and maxima of the density. However, since the wavepacket should remain zero at the boundary of the well, there is a point in time where diffusion stops and a second crest starts to form, with a half-moon shape, being thinner than the first one but larger in radius. At the same time, the vortex core itself keeps rotating (Fig. 1g) and the distortion of the phase excites new vortices, namely, a vortex-antivortex pair to conserve angular momentum (Fig. 1h). These are moving inside the fluid until their later recombination (Fig. 1i). Shortly after that, another vortex-antivortex pair is formed locally (Fig. 1j). Such processes are repeated during the full time evolution of the dynamics (See also the Supplementary Movie SM1 [23] for better illustration of the dynamics). Despite the complex motion of the core inside this fluid bouncing back and forth as it rotates inside the well, the angular momentum remains steady. This is expected since the external potential is a purely confining one, being radially symmetric and azimuthally homogeneous. Considering the potential gradient and its symmetry, its boundaries act both as a local and net force on the fluid at any moment, however there is no net torque acting on the fluid. Therefore, while the center of mass of the fluid and its net linear momentum keep changing due to the continuous bouncing of the fluid against the well boundaries, its net angular momentum remains constant. Yet, some peculiar morphology reshaping, involving also the topological charges, happens during the evolution. It is interesting to check how this is self-consistently ensured by the formalism which produces correspondingly intricate dynamics

of the fields:

$$\langle L_z \rangle = -i\hbar \int d\varphi \int r dr \psi^* \partial_\varphi \psi = \frac{\hbar R^2}{2} \sum_n |\alpha_{n,1}|^2 N_{n,1}^2 [J_2(\beta_{n,1})]^2. \quad (7)$$

Although the way the Bessel functions balance each others in space is not transparent, one can see indeed how Eq. (7) produces a time-independent average.

Another interesting quantity is the orbital angular momentum per particle, which in the case above is less than one, as expected for an off-center vortex [24], namely,  $\langle \tilde{L}_z \rangle \equiv \langle L_z \rangle / N < 1$ , with  $N$  the total number of particles<sup>1</sup>, given by

$$N = \frac{R^2}{2} \left[ \sum_n |\alpha_{n,1}|^2 N_{n,1}^2 [J_2(\beta_{n,1})]^2 + \sum_m |\alpha_{m,0}|^2 N_{m,0}^2 [J_1(\beta_{m,0})]^2 \right] \quad (8)$$

The condition  $\langle \tilde{L}_z \rangle < 1$  comes from the initial field (6), where we have introduced two kinds of particles with a fraction only of them carrying (integer and equal to one) angular momentum. The ratio of particles that carry angular momentum is responsible for the position of the core, making it closer to the center (less displaced) as more particles have angular momentum (i.e., for smaller  $a_c$ ). Similarly, increasing the number of particles without angular momentum (i.e., for larger  $a_c$ ) pushes the core towards the boundary.

Although both the total and mean value of the angular momentum is constant for the whole wavepacket, one can consider a local orbital angular momentum, which reveals time-varying features. In particular, we can define

$$\langle L_z \rangle_r \equiv -i\hbar \int_0^r \int_0^{2\pi} \rho \psi^* (\rho, \varphi, t) [\partial_\varphi \psi] (\rho, \varphi, t) d\varphi d\rho \quad (9)$$

the mean angular momentum enclosed in a circle of radius  $r$ , with  $\langle L_z \rangle = \lim_{r \rightarrow \infty} \langle L_z \rangle_r$ . Then the mean angular momentum on a circle of radius  $r$  is obtained as  $d\langle L_z \rangle_r / dr$ . Similarly, one can

<sup>1</sup>Also, in the next sections we refer to  $\langle \tilde{L}_z \rangle$  as the mean (expectational) value of orbital angular momentum per particle.

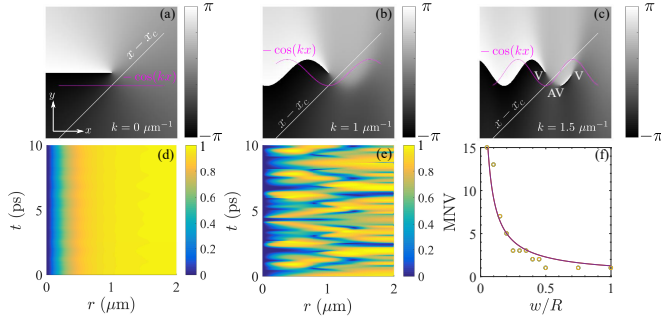


**Fig. 2.** Upper panels: toy-model for vortex-antivortex pair creation, caused by the phase distortion from the interference of two waves, one being oblique with respect to the other and carrying a topological charge  $TC \leq 1$ . The frames show different  $k$ , with increasing distortion of the phase. In (a) and (b) there is only one root, corresponding to the intersection of two curves  $x - x_c$  (shown in white) and  $-\cos(kx)$  (shown in magenta). In (c) there are three roots, bringing an additional vortex (V) and antivortex (AV). Panels (d) and (e) show the radial OAM per particle (defined in Eq. (10)) that quantifies angular momentum locally, showing how the orbital angular momentum, always constant in time, is also locally constant for large wavepackets, as in (d) with  $w = 5 \mu\text{m}$ ,  $a_c = 0.3$  and  $R = 2 \mu\text{m}$ , but displays a rich local time-dependence of the OAM, as in (e) with  $w = 0.5 \mu\text{m}$ . Panel (f) shows the maximum number of vortices (MNV) observed during the dynamics for different values of the wavepacket size  $w$ . The solid line is a (negative power law) fitting curve highlight the nonlinear dependence of MNV on the initial size  $w$ . Here we used  $a_c = 0.2$  and  $R = 2 \mu\text{m}$ .

define the mean number of particles on a circle of radius  $r$  as  $dN_r/dr$  with  $N_r = \int_0^r \int_0^{2\pi} \rho |\psi(\rho, \varphi, t)|^2 d\varphi d\rho$ , so that the chain rule yields the mean value of OAM per particle on a circle of radius  $\rho$ , that we call  $\langle \tilde{L}_z \rangle_r$ , as  $\langle \tilde{L}_z \rangle_r = \frac{d\langle \tilde{L}_z \rangle_\rho}{d\rho} \frac{d\rho}{dN_r}$ , which is thus given by:

$$\langle \tilde{L}_z \rangle_r = -i\hbar \frac{\int_0^{2\pi} d\varphi \psi^*(r, \varphi, t) [\partial_\varphi \psi](r, \varphi, t)}{\int_0^{2\pi} d\varphi |\psi(r, \varphi, t)|^2}. \quad (10)$$

This quantity is shown in panels d-e of Fig. 2 where it is seen how the local OAM exhibits strikingly different behaviours for different cases. For large  $w$ , with a smooth rotation of the field, the local angular momentum is constant in time on any radial distance from the center of the quantum well. However, by decreasing the initial packet size, which induces a nontrivial dynamics of the vortex, one then finds strongly time-varying features of the angular momentum but only locally, since these cancel when averaging over the entire wavepackets. This is shown in panel (e). At a given radius  $r$ , a torque can be felt locally due to the internal dynamics of the field, which is absent in panel (d). One can see that variations are stronger in the central part rather than close to the boundaries ( $r = 0, 2$ ), where the density of the field has less dynamics. This is clear from panels (c-d) of Fig. 1, where a half-moon shaped density near the boundary remains almost steady while the central part has a rich dynamics of vortex rotation and pair excitation.

The vortex-antivortex pair formation, evolution and later recombination, that all occur without affecting the total angular

momentum, but that can be detected locally, can be understood from the expanding cloud reaching the boundary and being reflected, producing a circular ripple of lower density and with a larger phase gradient (visible starting from Fig. 1b,g on). This interference between the outward diffusing and the inward reflected waves is the origin to the secondary vortex-antivortex pair, which is nucleated starting from this loop of locally low density. The pair creation can be modelled by using a toy-model which interferes two waves, both with a Laguerre Gaussian type envelope of same amplitude and propagating in the directions  $\mathbf{k}_1$  and  $\mathbf{k}_2 \neq \mathbf{k}_1$  as  $A_1 = e^{-i\mathbf{k}_1 \cdot \mathbf{r}} e^{-r^2/(2w^2)}$  and  $TC = 0$ ,  $A_2 = e^{-i\mathbf{k}_2 \cdot \mathbf{r}} e^{-r^2/(2w^2)} (r e^{i\varphi} - r_c e^{i\varphi_c})$ , with a TC. If, for simplicity,  $A_1$  travels along the  $x$  direction ( $\mathbf{k}_1 = k\hat{i}$ ) and  $A_2$  does not propagate ( $\mathbf{k}_2 = 0$ ), then the two interfering waves yield a total density  $I \propto |e^{ikx} + r e^{i\varphi} - r_c e^{i\varphi_c}|$ . The condition for a vanishing density is given as  $-\cos(kx) = x - x_c$  and  $-\sin(kx) = y - y_c$ . Depending on the wavenumber  $k$ , such a density can have either one or more roots. The former case corresponds to the initial topological charge  $TC \leq 1$ , while when there are three roots, a vortex-antivortex pair is added to the initial TC. An example for this behavior of the phase is shown in Fig. 2 a-c, where we take  $x_c = 1 \mu\text{m}$  and  $y_c = 0$  (obtained for the polar parameters  $r_c = 1 \mu\text{m}$  and  $\varphi_c = 0$ ). One can see how, upon increasing  $k$ , the phase gets distorted to the point of creating a vortex pair. This condition also depends on the relative amplitude of the two waves, which we did not consider to highlight the importance of the momentum. Coming back to the displaced vortex in the circular quantum well, the excitation of the pair comes into play when the reflected wave from the hard boundary interferes with the field inside the well, matching the toy-model above, where a vortex-antivortex pair is created and annihilated repeatedly. One could also consider higher-energy initial conditions with a larger number of vortex-antivortex pairs. The maximum number of vortices (MNV) observed during the dynamics as a function of the initial packet size  $w$  is shown in Fig. 2f. It is clear that by decreasing  $w$ , MNV is growing in a nonlinear fashion. Interestingly, also configurations of even number of vortices are possible, where a single vortex or antivortex can be excited from the boundary of the quantum well. In fact, since the distance of a vortex fractionalises its contribution to the OAM, and a pair of vortex/antivortex immediately drift apart with different distances, it is clear that the field itself must locally accommodate for the corresponding changing angular momentum, and it is thus not surprising that, would a vortex come from the boundary of the well, it is allowed to drift alone with no anti-counterpart without affecting the total OAM, which remains constant. These additional vortices and antivortices thus also display an intricate dynamics that also affects the morphology, which has to maintain a constant total and mean angular momentum. While we do not consider it here, nonlinearities also result in further vortex-antivortex dynamics with added complexity to the overall phenomenology.

### 3. HARMONIC POTENTIAL

Next, we consider the displaced vortex in a harmonic potential, so still with a confinement but that now grows quadratically with the distance from the center of the potential and thus with the possibility for the core to stray arbitrarily far from it. We will see that, surprisingly, such an opportunity is actually seized.



Schrödinger's equation  $i\hbar\partial_t\psi = H_{\text{ho}}\psi$  now has Hamiltonian

$$H_{\text{ho}} = -\frac{\hbar^2}{2m}\nabla^2 + \frac{1}{2}m\omega_{\text{ho}}^2 r^2, \quad (11)$$

with  $\omega_{\text{ho}}$  the natural frequency of harmonic oscillations. Ring potentials in general have been shown to sustain precessing vortices [25, 26] with conserved total OAM or even rotating patterns [27, 28], based on combinations of rotational modes of different eigenenergies. The harmonic potential provides the staple model for many vibrating systems. Here, we show interesting variations of the vortex fluid inside such potential in particular regarding the vortex core. We start our analysis with a displaced-vortex that is a spatial equipotential of the trap, that is to say, with a width parameter  $w = \beta \equiv \sqrt{\hbar/(m\omega_{\text{ho}})}$  that matches the potential's natural frequency:

$$\psi_0 = \frac{e^{-r^2/2w^2}}{w\sqrt{\pi(w^2 + r_c^2(0))}} (re^{i\varphi} - r_c(0)e^{i\varphi_c(0)}), \quad (12)$$

with  $(x_c(0) \equiv r_c(0) \cos \varphi_c(0), y_c(0) \equiv r_c(0) \sin \varphi_c(0))$  fixing the initial position of the core. Such a state, that is the VB version of a coherent state in the harmonic potential, could be implemented in an experiment with two delayed resonant pulses [17]. The wavepacket dynamics can be obtained in closed form as

$$\psi = \frac{e^{-r^2/(2\beta^2)} e^{-i\omega_{\text{ho}}t}}{\beta\sqrt{\pi(\beta^2 + r_c^2(0))}} [re^{i(\varphi - \omega_{\text{ho}}t)} - r_c(0)e^{i(\varphi_c(0))}]. \quad (13)$$

This gives the orbit described by the core, which is a circle of radius  $r_c(0)$ . Its motion proceeds with a constant speed  $v_c(0) = r_c(0)\omega_{\text{ho}}$ . Although the core oscillates in time, as previously and for the same reason, the total angular momentum content remains constant

$$\langle \tilde{L}_z \rangle = \hbar \frac{\beta^2}{\beta^2 + r_c^2(0)} = \hbar \left(1 - \frac{r_c^2(0)}{\beta^2 + r_c^2(0)}\right), \quad (14)$$

and fractional, which is consistent with an offset core. The value itself depends on the initial radial distance of the core, ranging from  $\langle \tilde{L}_z \rangle = 1$  for  $r_c(0) = 0$  to vanishing values as  $r_c(0)$  goes to infinity. Since the trajectory remains on a circle, this can be understood as another reason for, or a manifestation of, a constant angular momentum. In this case where the dynamics is smooth and simple, it is interesting to read more deeply into Eq. (14), that one can interpret as the total angular momentum arising as a combination of the TC = 1 (in units of  $\hbar$ ) and a field contribution  $-r_c^2(0)/(\beta^2 + r_c^2(0))$ . Interestingly, since the core itself is a clearly identified point (that of no density, or, even more clearly in cases of a weak background density, that of a phase singularity) with a well-defined position and velocity at all times, and since this core itself rotates, one can regard the core as a mechanical point with the hope of attaching to it the field contribution so that angular momentum is accounted in its entirety by the vortex core. To do so, one needs to provide an effective mass for the vortex core to define dynamical quantities such as its momentum (linear and angular) and its energy (kinetic and potential), according to the familiar expressions for a point-like particle in terms of the already known position  $\mathbf{r}_c$  and velocity  $\mathbf{v}_c$ . With the following choice for the core's effective mass,

$$m_c = -m \frac{\beta^2}{\beta^2 + r_c^2(0)}, \quad (15)$$

one can check that:

$$\langle L_z \rangle = \hbar + m_c(\mathbf{r}_c \times \mathbf{v}_c), \quad (16a)$$

$$\langle -i\hbar\nabla \rangle = m_c \mathbf{v}_c, \quad (16b)$$

$$\langle \frac{-\hbar^2\nabla^2}{2m} \rangle = \hbar\omega_{\text{ho}} + \frac{1}{2}m_c v_c^2, \quad (16c)$$

$$\langle \frac{1}{2}m\omega_{\text{ho}}^2 r^2 \rangle = \hbar\omega_{\text{ho}} + \frac{1}{2}m_c \omega_{\text{ho}}^2 r_c^2 \quad (16d)$$

where the left-hand sides of Eq. (16) are obtained as quantum average over the wavefunction (13) (with the mass involved  $m$  being that of the field) and the right-hand sides are classical expressions for a point-like Newtonian particle (with the mass involved being the effective one  $m_c$  for the vortex, Eq. (15)). Since Eq. (16b) is two equations (2D vector), one single definition of the effective mass fulfills five independent dynamical quantities, conferring to this object—the vortex core—a clear particle-like character. Note that one recovers the quantum results on the lhs by adding quanta to the classical expressions for the core on the rhs. This could be expected since the vortex defined as a mechanical point cannot carry the vacuum energy of the field, nor the topological charge, which are both inherently quantum or wavelike. Interestingly, the effective mass is negative and is “larger” (in magnitude) the closer to the center of the wavepacket, i.e., the more the depletion of the density. This explains neatly why the total angular momentum is fractional and less than the TC, which appears on its own as one quantum of angular momentum  $\hbar$ , as expected for a quantum vortex. Similarly, both the kinetic (16c) and potential (16d) energy for the core are defined in reference to the vacuum energy  $\hbar\omega_{\text{ho}}$ , which the core itself cannot be expected to carry in any classical form. As for the linear momentum, which has no intrinsic quantum component, the change of sign due to the negative mass can be understood as the core going in the opposite direction (in fact being radially opposite) to the wavefunction centroid itself, which carries the physical angular momentum.

This connection between quantum and classical pictures through the vortex itself also holds when the trajectories are not on equipotential lines but involve energy transfers between the kinetic and potential terms. This occurs when the initial condition is not spatially equipotential in the trap, that is, with  $w \neq \beta$ . The solutions are obtained as before

$$\psi = \sum_{nm} \alpha_{n,m}(t) \phi_{n,m}(x, y), \quad (17)$$

where  $H_{\text{ho}}\phi_{n,m} = E_{n,m}\phi_{n,m}$  and  $\alpha_{n,m}(t) = \int e^{-itE_{n,m}/\hbar} \psi_0 \phi_{n,m} dx dy$  with  $n, m = 0, 1, 2, \dots$ . The time-evolution of the density is shown in Fig. 3 for  $w = 0.7\beta$  and for the core located initially at  $(-\beta, 0)$ . The wavepacket first shrinks in size, while the core moves but now on an ellipse  $(x_c(t)/w)^2 + (wy_c(t)/\beta^2)^2 = (\beta/w)^2$  rather than on a circle, with  $\mathbf{r}_c = (x_c, y_c)$  and  $\mathbf{v}_c = d\mathbf{r}_c/dt$  obtained as:

$$\mathbf{r}_c = -\beta \cos(\omega_{\text{ho}}t) \hat{i} - \frac{\beta^3}{w^2} \sin(\omega_{\text{ho}}t) \hat{j}, \quad (18a)$$

$$\mathbf{v}_c = \beta\omega_{\text{ho}} \sin(\omega_{\text{ho}}t) \hat{i} - \frac{\beta^3\omega_{\text{ho}}}{w^2} \cos(\omega_{\text{ho}}t) \hat{j}. \quad (18b)$$

Note as well that the speed is now nonuniform. The wavepacket recovers its initial size as the core completes one period of its motion. Such oscillations are repeated during the time evolution of the dynamics. Apart from the peculiar motion of the vortex core, with accelerations and decelerations along an ellipse, and

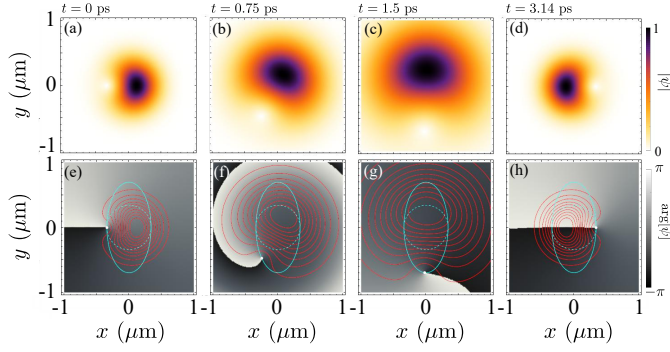


**Fig. 3.** Density plot (upper panels) and phase map (lower panels) of a displaced vortex in the non-equipotential case ( $w = 0.7\beta$ ) of a symmetric harmonic potential. The trajectory of the core is an ellipse shown in solid cyan line (the trajectory for the equipotential ( $w = \beta$ ) case is also shown in dashed circle line, for comparison). The vortex morphology is shown with red isocontours  $|\psi| = \text{constant}$  in the phase maps.

with also an intricate time-varying morphology of the phase, the quantum average of angular momentum is still constant since in general, and for any initial condition, the expectation value of angular momentum reads as

$$\langle L_z \rangle_{\text{ho}} = i\hbar \sum_{n,m} \alpha_{nm}^*(0) [\alpha_{n-1,m+1}(0) \sqrt{n(m+1)} - \alpha_{n+1,m-1}(0) \sqrt{m(n+1)}], \quad (19)$$

which is, again, clearly time-independent. This too (like in the case of the circular quantum well) is expected from the symmetry of the radial force field (energy gradient) of such a potential, which has a zero net torque. In its interaction with the fluid, it cannot exert any change of its overall angular momentum, which therefore remains. In contrast, the phase morphology and the core, both also tightly connected to the angular momentum, have a nontrivial time dynamics. This is satisfied by the core as a mechanical point with now Keplerian compensation between its distance  $r_c$  and velocity  $\mathbf{v}_c$  in their vector product from the right-hand side of Eq. (16a). Linear momentum (16b) reads the same and Eqs. (16c–16d) need to have  $\hbar\omega_{\text{ho}}$  upgraded to  $\hbar\omega_{\text{ho}} \left( \left( \frac{\beta}{w} \right)^\sigma \cos^2(\omega_{\text{ho}}t) + \left( \frac{w}{\beta} \right)^\sigma \sin^2(\omega_{\text{ho}}t) \right)$  with  $\sigma = 2$  for the kinetic energy and  $\sigma = -2$  for the potential energy. Such classical/quantum relationships for the core and its wavefunction could be pushed further but, more interestingly and for the present discussion, we point out that they break, at least in this form, when the dynamics of the core becomes clearly nonclassical.

To exhibit such a case, we now introduce a perturbation that triggers a time dynamics of the angular momentum. Namely, we add a spatial anharmonicity in the form of a quartic contribution added to the harmonic oscillator potential. Indeed, a fluid in a power law trap demonstrated rich vortex states including crossover from vortex lattice to a giant vortex [29]. We do not consider such transitions at large rotational velocities here, as we rather focus on the onset of a time-varying angular momentum due to the anharmonicity, which could be naturally present in any vibrating system. Here, for simplicity, we consider an anisotropic anharmonic term  $H_{an} \equiv \lambda x^4$ , with  $\lambda > 0$ . In this

case, coefficients  $\alpha_{n,m}$  are given by:

$$\alpha_{n,m}(t) = e^{-it(E_{n,m} + \lambda\gamma_{n,m})/\hbar} \left( \alpha_{n,m}(0) - i \frac{\lambda}{\hbar} \int_0^t dt' e^{it'(E_{n,m} + \lambda\gamma_{n,m})/\hbar} \sum_{n' \neq n} \alpha_{n,n'}(t') \gamma_{n',n} \right), \quad (20)$$

where  $\gamma_{n',n} \equiv \langle \phi_{n',k} | x^4 | \phi_{n,k} \rangle$ . Due to the parity of the eigenstates  $\phi_{n,m}$ , nonzero values of  $\gamma_{n',n}$  are given for  $n + n'$  equal to an even nonzero integer. This simplifies the computation of  $\alpha_{n,m}(t)$ . While the angular momentum is constant for the harmonic potential, even a small deviation, such as the anisotropic anharmonicity that we have introduced, can result in a time-varying angular momentum. Clearly, the force field is not central anymore and can now participate to the rotation of the fluid as a whole. Taking as an initial condition  $w = \beta$  in Eq. (12), the anisotropic anharmonicity removes the degeneracy of the excited states of the harmonic potential, and even for small  $\lambda$ , the wavepacket in Eq. (13) assumes a qualitatively different form. Namely, it now reads as

$$\psi = \frac{e^{-r^2/(2\beta^2)} e^{-i(\omega_{\text{ho}} + \gamma_0)t}}{\beta \sqrt{\pi(\beta^2 + r_c^2(0))}} \left[ e^{-i\omega_{\text{ho}}t} (x + iy e^{-i(\gamma_1 - \gamma_0)t}) - r_c(0) e^{i(\varphi_c(0))} \right], \quad (21)$$

where we have introduced  $\gamma_n \equiv \lambda\gamma_{n,n}/\hbar$ . This induces a time-varying angular momentum which reads as:

$$\langle \tilde{L}_z \rangle = \hbar \frac{\beta^2}{r_c^2(0) + \beta^2} \cos(t(\gamma_1 - \gamma_0)), \quad (22)$$

that is, with an angular momentum that not only oscillates in time but also change signs. The amplitude of oscillations is bounded in a  $(-\hbar, \hbar)$  interval. The core now evolves on the following orbits, which correspond to boomerang shapes:

$$x_c(t) = r_c(0) \sec((\gamma_1 - \gamma_0)t) \cos((\omega_{\text{ho}} + \gamma_1 - \gamma_0)t + \varphi_c(0)), \quad (23a)$$

$$y_c(t) = r_c(0) \sec((\gamma_1 - \gamma_0)t) \sin((\omega_{\text{ho}} + \gamma_1 - \gamma_0)t + \varphi_c(0)), \quad (23b)$$

Examples of the dynamics are shown in Fig 4. The vortex core (white dot) moves on two disconnected boomerang trajectories (shown in cyan) as it shapes the morphology of the vortex phase, which is shown with the red contours. The most striking departure brought by this case is that the core now can escape to infinity (Fig 4a-c), and reappears on another branch (Fig 4d-g). When the vortex is infinitely far, the phase morphology is uniform and the total angular momentum is zero. This thus also corresponds to the point where angular momentum changes sign. This is a nice illustration of a complex topological inversion imparted by even a possibly weak anharmonicity. Such topological inversions have been reported before with free linear propagation [30, 31] and we hereby provide a counterpart rooted in rotation (and with a potential, in Section 5 we also provide a case in free space). While the reversal of the total angular momentum in itself is not a wave-feature of the model, as it is also produced by a classical oscillator, the behaviour of the core, which is also more striking, is peculiar to the topological character of the VB. The cycles are also repeated forever. Moreover, one can observe an edge dislocation, that is, when  $t_{\text{cr}} \equiv \mathcal{N}\pi/[2(\gamma_1 - \gamma_0)]$ , with  $\mathcal{N}$  an integer. Indeed, the overall

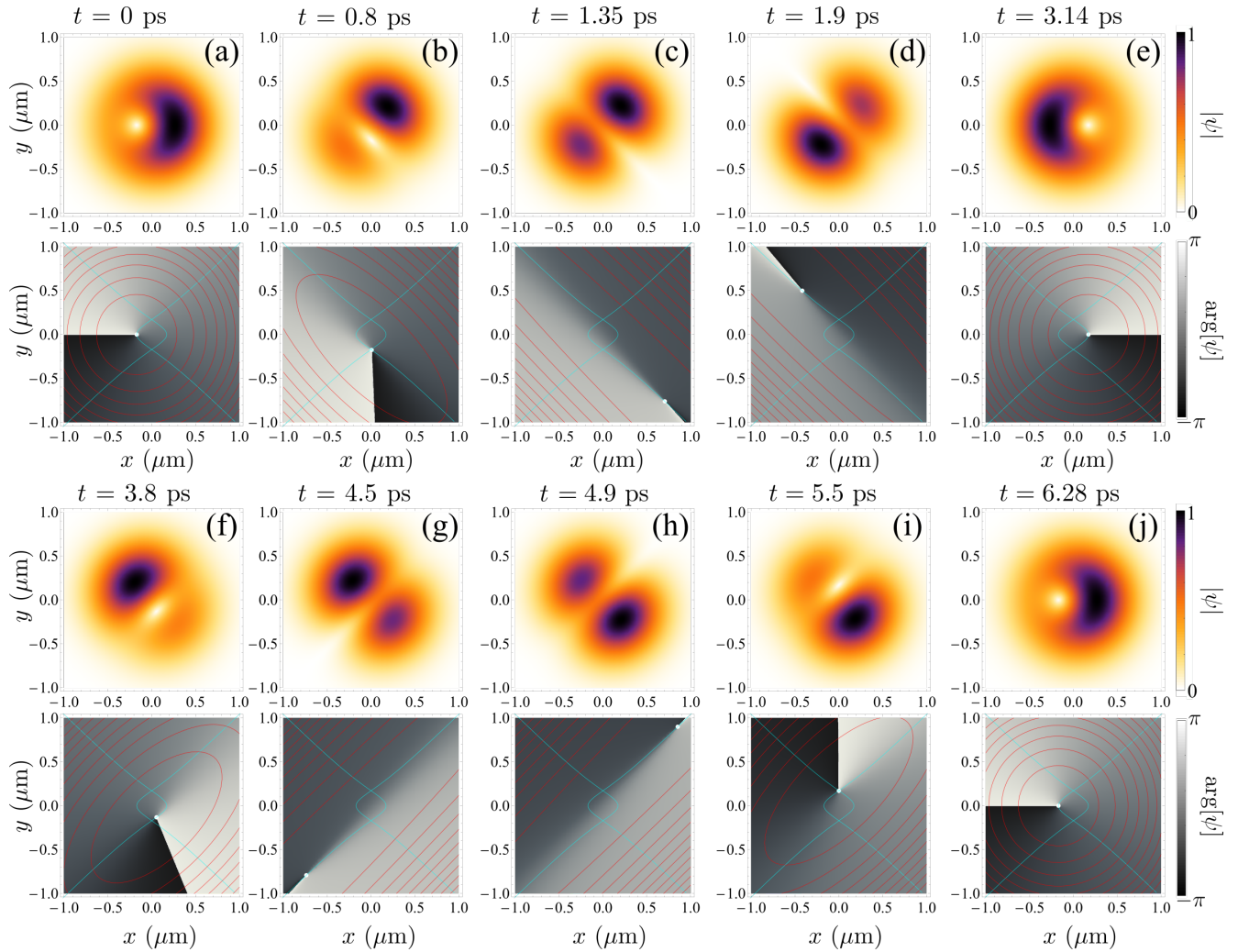


**Fig. 4.** Frames of the dynamics of a displaced-vortex in the presence of a quartic anharmonicity in one direction of the 2D oscillator, highlighting a case of a VB with time-varying angular momentum. The two sets of panels show density and phase of the wavefunction at different time frames. The core (white dot) moves on a boomerang-shape trajectories (cyan). As it is sent to infinity on one branch, it reappears on the other branch. Density maps and isodensity contours (red lines) in the phase maps show the vortex morphology, which is periodically stretched and folded up. The lines evolve from circles at  $t = 0$  in (a) to ellipses ((b) and (f)) which get stretched into parallel straight lines when angular momentum vanishes and the core is sent to infinity. Parameters:  $w = \beta$ ,  $\omega_{ho} = 1 \text{ ps}^{-1}$ .

movement of the fluid consists of an additional left and right oscillation due to the anisotropic term along this direction, in addition to also moving up and down due to the harmonic trap. This causes dark interference lines along the diagonal directions, which are reminiscent from the crossing lines between the two terms of the potential. Notably, these diagonal edge dislocations are the most pronounced when the vortex core is at infinity. As pointed out earlier, for a core that exhibits such an unfamiliar dynamics as far as any mechanical point-like object is concerned, relationships such as Eqs. (16) do not hold anymore, with no effective mass being able to account simultaneously for all the Newtonian expressions of the dynamical quantities.

#### 4. SQUEEZED HARMONIC POTENTIAL

We now consider a displaced vortex in a squeezed harmonic potential, where the trap is harmonic, so representing another linear system, but with a broken symmetry by the trap that arises

from its anisotropic confinement in the two directions. This also gives rise to an interesting and counter intuitive dynamics of the vortex core, with time varying angular momentum, similar to the nonlinear case above, although now in a fully linear system. The external potential thus now reads as:

$$H_{SQ} = -\frac{\hbar^2}{2m} \nabla^2 \psi + \frac{1}{2} m (\omega_x^2 x^2 + \omega_y^2 y^2), \quad (24)$$

where  $\omega_x \neq \omega_y$  (squeezing) provide the natural frequencies in the  $x$  and  $y$  directions, respectively. As previously, the vortex solutions are found by solving  $i\hbar \partial_t \psi = H_{SQ} \psi$ , with eigenstates and eigenenergies of  $H_{SQ}$  being found as

$$\varphi_{n,m} = \frac{e^{-((x/\beta_x)^2 + (y/\beta_y)^2)/2}}{\sqrt{\beta_x \beta_y} \sqrt{\pi 2^{n+m} n! m!}} H_n(x/\beta_x) H_m(y/\beta_y), \quad (25a)$$

$$E_{nm} = \hbar \left( \omega_x \left( n + \frac{1}{2} \right) + \omega_y \left( m + \frac{1}{2} \right) \right), \quad (25b)$$



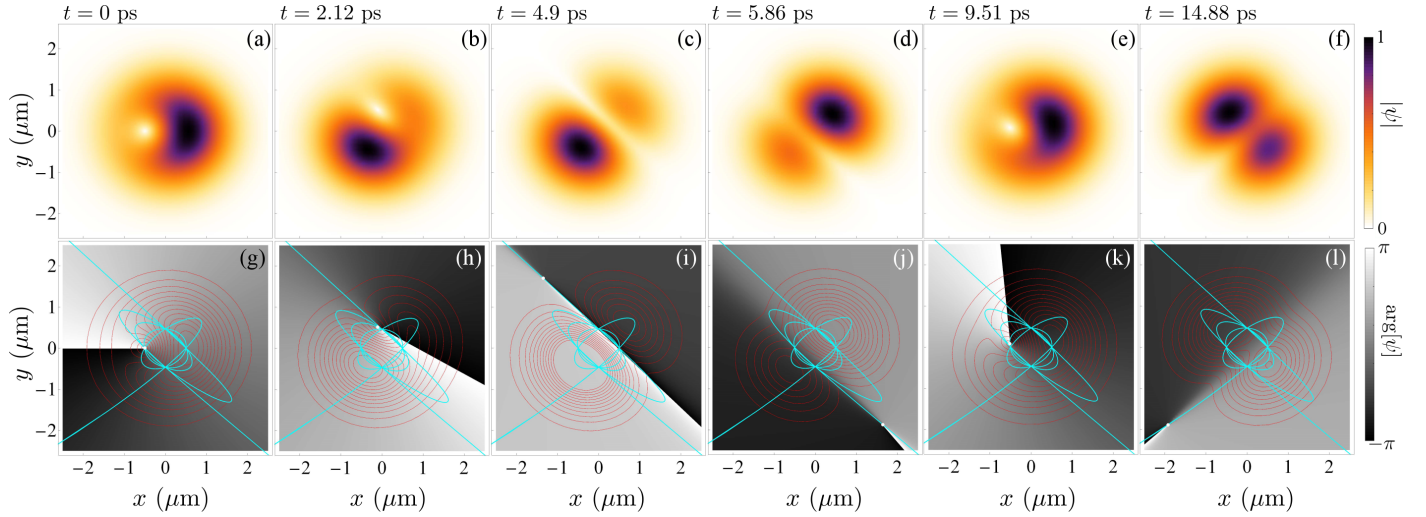


**Fig. 5.** Frames of the dynamics of a displaced vortex in a squeezed harmonic potential, with differing confinement in two directions. Upper row (a-f) shows the density plot of the field ( $|\psi|$ ). Lower row (g-l) shows the phase map of the field, with isocontours (in red) of the density. The orbit of the core is shown in cyan, with two branches going to infinity. Parameters:  $\omega_x = 2 \text{ ps}^{-1}$ ,  $\omega_y = 2.3 \text{ ps}^{-1}$ ,  $x_c = -0.5 \text{ } \mu\text{m}$ ,  $y_c = 0$ .

where  $\beta_{x,y} = \sqrt{\hbar/m\omega_{x,y}}$ . The vortex solution is then expressed as  $\psi = \sum_{n,m} \alpha_{n,m}(0) e^{-i\frac{E_{n,m}}{\hbar}t} \varphi_{n,m}(x,y)$  where  $\alpha_{n,m}(0) = \int \psi_0(x,y,0) \varphi_{n,m}(x,y)$ . Given  $\psi_0$  as the initial wavepacket for a displaced vortex:

$$\psi_0(x,y,0) = C e^{-((x/\beta_x)^2 + (y/\beta_y)^2)/2} \left( \frac{x - x_c(0)}{\beta_x} + i \frac{y - y_c(0)}{\beta_y} \right), \quad (26)$$

with  $C \equiv \frac{(\beta_x \beta_y)^{-1/2}}{\sqrt{\pi(1 + (x_c(0)/\beta_x)^2 + (y_c(0)/\beta_y)^2)}}$ , the subsequent dynamics of the VB is given by

$$\psi(x,y,t) = C e^{-i(\omega_x + \omega_y)t/2} e^{-((x/\beta_x)^2 + (y/\beta_y)^2)/2} \times \left( \beta_x^{-1} (x e^{-i\omega_x t} - x_c(0)) + i \beta_y^{-1} (y e^{-i\omega_y t} - y_c(0)) \right). \quad (27)$$

It is remarkable that such a trivial-looking solution leads to the rich and counter-intuitive dynamics that we describe in the following. We provide an example of it in Fig 5. Initially the vortex core is located at  $(x_c = -0.5, y_c = 0)$  and starts to move counterclockwise with a non-uniform speed. As it accelerates, the core is forced to leave the density cloud and travels at the periphery of the beam after a few rotations. Since this is a topological feature, it cannot disappear altogether even if ejected from the fluid. As was the case for the anharmonic oscillator, there comes a point in time when the core is sent away at infinity, in our case along a diagonal in the  $x > 0$  part of the plane, coming back from the opposite quadrant with respect to the one from which it leaved the plane. The comeback is done with a deceleration similar to the acceleration of escape, and as the core comes back to its initial position, the cycle can repeat, now in the opposite sense of rotation and escaping along the diagonal of previous return. Without dissipation, this cyclical dynamics is sustained forever. The dynamics is also highlighted in a supplementary Movie SM2 [32]. The trajectory of the core is

obtained from Eq. (27) as:

$$\mathbf{r}_c \equiv \sec(\omega_r t) \left[ x_c(0) \cos(\omega_x t) - y_c(0) \sqrt{\frac{\omega_y}{\omega_x}} \sin(\omega_y t) \right] \hat{i}, \\ + \sec(\omega_r t) \left[ y_c(0) \cos(\omega_x t) + x_c(0) \sqrt{\frac{\omega_x}{\omega_y}} \sin(\omega_y t) \right] \hat{j}, \quad (28)$$

where an envelope of the form of  $\sec(\omega_r t)$  is superimposed to the otherwise simply elliptical oscillation, and  $\omega_r = \omega_x - \omega_y$ . The velocity follows straightforwardly by taking the time derivative. As before, this term can bring the core to infinity, with extreme accelerations. Depending on the ratio of  $\zeta \equiv \omega_y/\omega_x$  and the initial position of the vortex core  $(x_c(0), y_c(0))$  the singularity of the secant function may be removed. For example, when  $x_0 = 0$  and  $\zeta = (2k \pm 1)/2k$  with  $k$  as a positive integer, the vortex core does not go to infinity and stays on a bound orbit, with a stopping point at the end of each cycle where the motion decelerates and accelerates in the opposite direction. The vortex core coordinates themselves,  $(x_c(t), y_c(t))$ , obey the following equations:

$$\frac{d^2 x_c}{dt^2} = (-\omega_y^2 + \omega_r^2) x_c(t) + 2 \frac{dx_c}{dt} \omega_r \tan \omega_r t, \quad (29a)$$

$$\frac{d^2 y_c}{dt^2} = (-\omega_x^2 + \omega_r^2) y_c(t) + 2 \frac{dy_c}{dt} \omega_r \tan \omega_r t, \quad (29b)$$

showing how their natural oscillations are at the frequencies  $\omega_{x,y}^2 - \omega_r^2$  but with forceful accelerations ( $\tan \omega_r t > 0$ ) and decelerations ( $\tan \omega_r t < 0$ ) under the effect of the second term which is proportional to the speed of the core. This term is induced by the different frequencies  $\omega_r \neq 0$  along the  $x$  and  $y$  axis, i.e., by the squeezing of the trap. The time-varying angular momentum can also be obtained exactly from Eq. (27), as

$$\langle \bar{L}_z \rangle = \frac{\hbar}{2} \pi C^2 (\beta_x^2 + \beta_y^2) \cos \omega_r t, \quad (30)$$

which also makes transparent how the squeezing from the potential induces time variations of the total angular momentum.



Importantly, the field dynamics is fairly different depending on whether the vortex is displaced or not. Indeed, for axially symmetric VB ( $x_c = y_c = 0$ ), the density of the field does not rotate, in contrast to the off-centered case ( $x_c \neq 0$  and/or  $y_c \neq 0$ ) with a clear rotation of the field, as shown in Fig. 5. Here too, there is an interesting topological switching, that is, when  $(2\mathcal{N} - 1)\pi < 2t\omega_r < (2\mathcal{N} + 1)\pi$  for  $\mathcal{N}$  a positive odd integer, the angular momentum of the field is positive, while for positive even integers, it is negative. Like for the anharmonic case from the previous section, the core, which even in such a simple system can be brought to extreme behaviours, cannot be described as a mechanical point-like object with an effective mass to account by itself for the dynamical properties of the full field. It remains well-identified as far as its kinematics is concerned, with an unambiguous position and velocity at all times, but this does not fit with classical equations of motion. This puts forward interesting questions on the nature of a vortex and the conditions sufficient and/or necessary to reduce it to a particle-like object.

## 5. RABI-COUPLED FIELDS

We conclude with the case which inspired all the others considered previously, since its experimental observation by Dominici *et al.* [17] triggered our interest into the underlying mechanism, that we have now generalized to several systems. While we will focus on polaritons, other similar systems, such as spin-orbit coupled BEC [33], could also accommodate these results. Rabi-coupled fields [34] also exhibit time-varying angular momentum, this time without any external potential (in free two-dimensional space) but activated for each field by its coupling to the other. The system is described by a coherent coupling between two fields  $\psi_C$  and  $\psi_X$ , describing a cavity-photon field and a quantum-well excitonic field, respectively, in strong-coupling [19], with equations that correspond to two coupled Schrödinger equations:

$$i\hbar\partial_t \begin{pmatrix} \psi_C(x, y, t) \\ \psi_X(x, y, t) \end{pmatrix} = \mathcal{L} \begin{pmatrix} \psi_C(x, y, t) \\ \psi_X(x, y, t) \end{pmatrix}, \quad (31)$$

where

$$\mathcal{L} = \begin{pmatrix} -\frac{\hbar^2\nabla^2}{2m_C} + E_C & \hbar\Omega \\ \hbar\Omega & -\frac{\hbar^2\nabla^2}{2m_X} + E_X \end{pmatrix}. \quad (32)$$

Here,  $\Omega$  is the Rabi frequency which couples the two fields with respective free energies  $E_{C,X}$  and masses  $m_{C,X}$ . There are typically decay terms to describe such particles which, however, we do not need to consider for our present discussion, although they also lead to interesting variations of the dynamics. As previously, we assume for the initial condition a displaced core, albeit now with one vortex in each field:

$$(\psi_{C,X})|_{t=0} = \frac{e^{-r^2/2w^2}}{w\sqrt{\pi(w^2 + r_{c,x}^2)}} (re^{i\varphi} - r_{c,x}e^{i\varphi_{c,x}}). \quad (33)$$

The vortex cores are located at possibly different points in real space, defined by  $(r_{c,x}, \varphi_{c,x})$  in polar coordinates. One can find a closed-form solution in reciprocal space ( $k = \sqrt{k_x^2 + k_y^2}$  and  $\theta_k = \arg[k_x + ik_y]$ ) by turning to the Fourier-transform  $\mathcal{F}$  of each field,

which yields a general expression for the amplitudes of the two coupled fields:

$$\begin{aligned} \tilde{\psi}_C &= \frac{1}{k_\Omega^2} e^{-i\frac{(k\lambda)^2 M_\pm t}{2\hbar}} \\ &\times \left[ -i \sin\left(\frac{k_\Omega^2 t}{2\hbar}\right) \left( 2\hbar\Omega(\tilde{\psi}_X)|_{t=0} + (\tilde{\psi}_C)|_{t=0}(\hbar\delta + (k\lambda)^2 M_-) \right) \right. \\ &\left. + (\tilde{\psi}_C)|_{t=0} k_\Omega^2 \cos\left(\frac{k_\Omega^2 t}{2\hbar}\right) \right], \end{aligned} \quad (34a)$$

$$\begin{aligned} \tilde{\psi}_X &= \frac{1}{k_\Omega^2} e^{-i\frac{(k\lambda)^2 M_\pm t}{2\hbar}} \\ &\times \left[ -i \sin\left(\frac{k_\Omega^2 t}{2\hbar}\right) \left( 2\hbar\Omega(\tilde{\psi}_C)|_{t=0} - (\tilde{\psi}_X)|_{t=0}(\hbar\delta + (k\lambda)^2 M_-) \right) \right. \\ &\left. + (\tilde{\psi}_X)|_{t=0} k_\Omega^2 \cos\left(\frac{k_\Omega^2 t}{2\hbar}\right) \right], \end{aligned} \quad (34b)$$

with  $\tilde{\psi}_{C,X} = \mathcal{F}[\psi_{C,X}]$  and where we introduced  $M_\pm \equiv \frac{\hbar\Omega}{2} (1 \pm (m_C/m_X))$ ,  $\lambda \equiv \sqrt{\hbar/m_C\Omega}$ , and  $k_\Omega^2 = \sqrt{(2\hbar\Omega)^2 + (\hbar\delta + (k\lambda)^2 M_-)^2}$  with  $\hbar\delta \equiv E_C - E_X$  the energy detuning. In general, it is not possible to find the corresponding closed-form solution in real space, due to the polaritonic factor [35], caused by the mass imbalance. For equal masses of the exciton and photon fields,  $k_\Omega$  is constant and the dispersion plays no role. One can then find exact solutions as shown below. These remain excellent approximations over several periods of the phenomenon when the  $k$  dependence of  $k_\Omega$  is small as compared to the Rabi coupling. At zero detuning, for instance,  $k_\Omega = (2\hbar)^{(1/4)}\sqrt{\Omega}$  for equal masses and a similar situation holds for different masses when  $k \ll \sqrt{4m_C\Omega/[\hbar(1 - m_C/m_X)]}$ . Since the spread in  $k$  is related to the packet size  $w$ , one can transpose this condition to read

$$w \gg \sqrt{\frac{\hbar(1 - m_C/m_X)}{2m_C\Omega}}. \quad (35)$$

In the limit of a very large mass imbalance, as is typically the case, this yields  $w \gg \sqrt{\hbar/(2m_C\Omega)}$ , whose right-hand-side evaluates to about half a micron for standard parameters, showing that the approximations below are actually enforced by the diffraction limit for well over the entire duration of the observations for typical lifetimes of the particles [17]. Therefore, assuming from now on no effect of the dispersion and taking  $k_\Omega^2 \approx \sqrt{(2\hbar\Omega)^2 + (\hbar\delta)^2}$ , expanding the expression for the fields (34) and considering the initial condition of two displaced vortices (33), we find

$$\begin{aligned} \psi_C &\approx \frac{we^{i\varphi}\lambda^2 - 2iw^2}{t\Omega'\lambda^2 - 2iw^2} \left[ \frac{2i\Omega \sin \omega_R t}{\omega_R \sqrt{\pi(w^2 + r_x^2)}} \left( \frac{2w^2 re^{i\varphi}}{t\Omega'\lambda^2 - 2iw^2} - ir_x e^{i\varphi_x} \right) \right. \\ &\left. + \frac{2w^2 re^{i\varphi}}{t\Omega'\lambda^2 - 2iw^2} - ir_c e^{i\varphi_c} \right] \left( \frac{i\delta \sin \omega_R t}{\omega_R} - 2 \cos \omega_R t \right), \end{aligned} \quad (36a)$$

$$\begin{aligned} \psi_X &\approx \frac{we^{i\varphi}\lambda^2 - 2iw^2}{t\Omega'\lambda^2 - 2iw^2} \left[ \frac{2i\Omega \sin \omega_R t}{\omega_R \sqrt{\pi(w^2 + r_x^2)}} \left( \frac{2w^2 re^{i\varphi}}{t\Omega'\lambda^2 - 2iw^2} - ir_c e^{i\varphi_c} \right) \right. \\ &\left. + \frac{2w^2 re^{i\varphi}}{t\Omega'\lambda^2 - 2iw^2} - ir_x e^{i\varphi_x} \right] \left( \frac{-i\delta \sin \omega_R t}{\omega_R} - 2 \cos \omega_R t \right), \end{aligned} \quad (36b)$$

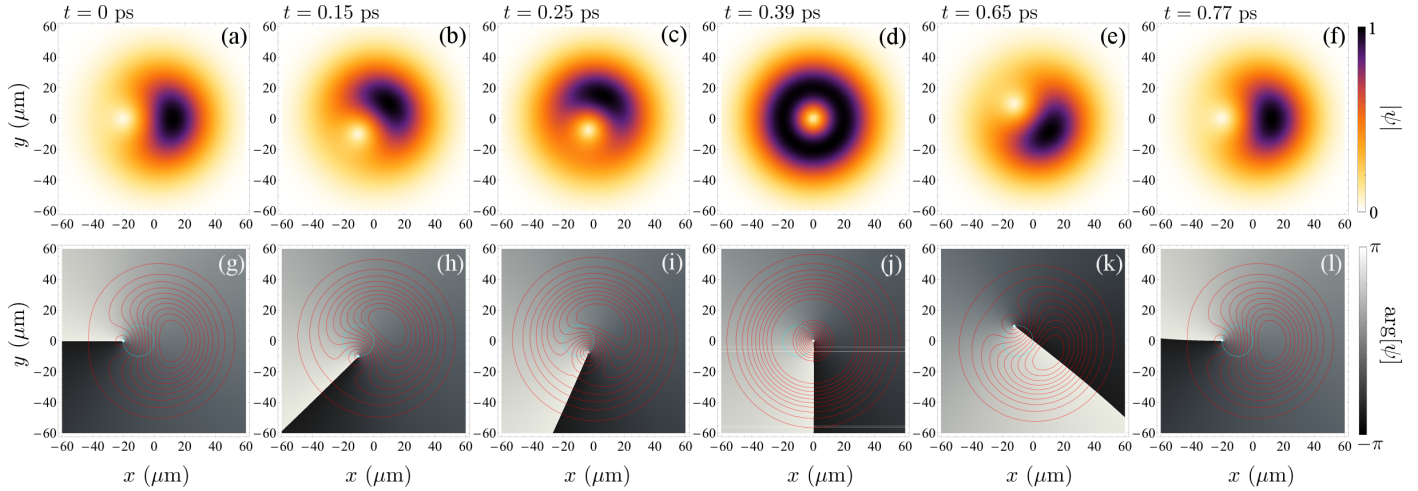


**Fig. 6.** Density plot and phase map in the photon field of a Rabi-coupled system with a displaced vortex in each field. The core is initially located at  $(-w, 0)$  and in the limit of  $m_C/m_X = 0.001 \ll 1$  for  $\psi_C$  in Eq. (36a). The position of the core is shown by a white dot, its trajectory in cyan and the red contours show the shape (morphology) of the corresponding vortex beam.

where  $\omega_R \equiv \sqrt{(2\Omega)^2 + \delta^2}/2$  is the natural frequency of the coupled system, and  $\Omega' \equiv \Omega(1 + m_C/m_X)$ . Note that, if initially the two vortex cores are positioned at the same point in space ( $r_c e^{i\varphi_c} = r_x e^{i\varphi_x}$ ) in their respective fields, they do not move at all. However, detuning ( $\delta \neq 0$ ) can induce phase-driven oscillations of the density [35–37], with the morphology either remaining constant, or otherwise undergoing a complex orbiting reshaping. The mean total angular momentum per particle for each field is given as <sup>2</sup>:

$$\begin{aligned} \langle \tilde{L}_z \rangle_{C,X} = & \frac{\hbar w^2}{4} \left[ \frac{4 \cos^2 \omega_R t}{w^2 + r_{c,x}^2} + \frac{\sin^2 \omega_R t}{\omega_R^2} \left( \frac{(2\Omega)^2}{w^2 + r_{x,c}^2} \right. \right. \\ & \left. \left. \pm \frac{4\Omega\delta}{\sqrt{(w^2 + r_c^2)(w^2 + r_x^2)}} + \frac{\delta^2}{w^2 + r_{c,x}^2} \right) \right] / \\ & \left[ \cos^2 \omega_R t + \frac{(\delta^2 \pm \frac{4\delta\Omega(r_c r_x + w^2)}{\sqrt{r_c^2 + w^2} \sqrt{r_x^2 + w^2}} + 4\Omega^2) \sin^2 \omega_R t}{4\omega_R^2} \right], \end{aligned} \quad (37)$$

which is clearly independent of the mass imbalance  $m_C/m_X$ , and is also oscillatory in time. Again, it can be observed that for co-aligned vortices at zero detuning, the momentum stays constant. If however  $\delta \neq 0$ , even though the cores do not move, there are some spatial density waves and angular momentum oscillations induced by the detuning.

In the more general case where the two vortices are not aligned, thereby exhibiting a relative displacement one to the other, they exhibit some of the displaced-vortex dynamics of the previous sections. The two vortex cores also orbit each other. Angular momentum, alongside density, is coherently transferred and oscillating between the two fields. The net total angular momentum, obtained as the sum of angular momentum of the two fields, is conserved. The total angular momentum in each field, however, is time-dependent. Note that the observation of the system is typically performed over one field only (the photon field), so this polaritonic mechanism is intrinsically one that generates periodically time-varying OAM. It originates from the exchange

<sup>2</sup>The equation is written by assuming for simplicity in the initial condition that  $\varphi_c = \varphi_x$  without losing generality.

of particles with different positions and momenta [36, 37], as is well represented by the cores moving in their off-axis orbits (which are also periodically changing their distances from the center). An example of this polaritonic dynamics is shown in Fig. 6 for  $m_C/m_X \ll 1$ , with frames of the density and phase maps for the photon ( $\psi_C$ ) field (see also supplementary Movie SM3 in [38]). The core moves along a circular orbit, shown in cyan, and the morphology of the vortex, further shown by red isodensity contours, also displays the type of nontrivial oscillatory structure similar to those already encountered in the previous systems. Here too, the core and the fluid as a whole exhibit peculiar and opposed dynamics, with the core undergoing sequences of accelerations and decelerations, being faster in the outer part of the beam [17, 35], while the angular momentum oscillates smoothly and regularly. The essence of this behaviour can be reproduced by a simplified version of the coupled field solutions, namely, in matrix representation (cf. appendix A):

$$\begin{pmatrix} \psi_C \\ \psi_X \end{pmatrix} = \mathcal{J} \begin{pmatrix} (\psi_C)|_{t=0} \\ (\psi_X)|_{t=0} \end{pmatrix}, \quad (38)$$

with

$$\mathcal{J} \equiv \begin{pmatrix} \cos \omega_R t - \frac{i\delta}{2\omega_R} \sin \omega_R t & -\frac{i\Omega}{\omega_R} \sin \omega_R t \\ -\frac{i\Omega}{\omega_R} \sin \omega_R t & \cos \omega_R t + \frac{i\delta}{2\omega_R} \sin \omega_R t \end{pmatrix}. \quad (39)$$

Again, solutions (38–39) are valid in the regime when  $w \gg 1$  only, and would break down for example, when effects from the dispersion play a role [39]. In this case further noteworthy dynamics takes over, with vortex-antivortex pair creation and recombination similar to the circular quantum well discussed above, but those are beyond the current scope of this text. The representation (39) evokes a rotation matrix, however, it differs due to the complex elements. Such a unitary matrix is familiar from the dynamics of binary fields in the linear regime [37] and although it differs from a mere rotation matrix, it bears an interpretation similar to rotation. To show this, we introduce a complex number that defines the quantum state in the basis of the coupled fields  $\mathcal{Z} \equiv \psi_C/\psi_X$ . The matrix representation in

Eqs. (38-39) reappears as a bilinear transformation  $\mathcal{Z}_0 \mapsto \mathcal{Z} = M(\mathcal{Z}_0)$ , where  $\mathcal{Z}_0$  is the initial state, with

$$M \equiv \frac{\mathcal{Z}_0 \left( \cos \omega_R t - \frac{i\delta}{2\omega_R} \sin \omega_R t \right) - \frac{i\Omega}{\omega_R} \sin \omega_R t}{\mathcal{Z}_0 \left( \frac{-i\Omega}{\omega_R} \sin \omega_R t \right) + \cos \omega_R t + \frac{i\delta}{2\omega_R} \sin \omega_R t}. \quad (40)$$

Assuming  $\delta = 0$  hereafter for simplicity, the transformation (40) has two fixed states  $\mathcal{Z}_0 = \pm 1$ , which correspond to the vortex cores in the dressed states (eigenstates, or normal modes)<sup>3</sup>. Rewriting the transformation  $M$  in the normal form:

$$\frac{\mathcal{Z} - 1}{\mathcal{Z} + 1} = e^{2i\Omega t} \frac{\mathcal{Z}_0 - 1}{\mathcal{Z}_0 + 1} \quad (41)$$

one finds that any  $\mathcal{Z}$  is mapped in the complex plane and evolves with a time-dynamics that keeps it on Apollonius circles [17], which are symmetric with respect to the fixed points, and that  $M$  maps each such circle in this plane to itself. In advanced complex analysis, the specific transform  $M$  is an example of an elliptic transform [40]. This makes  $\mathcal{Z}$  points the images in a plane of their respective location on a Riemann sphere through a stereographic projection. Denoting a point on the Riemann sphere as  $(X, Y, Z)$ , the stereographic expressions is given by:

$$X + iY = \frac{2\mathcal{Z}}{1 + |\mathcal{Z}|^2}, \quad (42a)$$

$$Z = \frac{|\mathcal{Z}|^2 - 1}{|\mathcal{Z}|^2 + 1}. \quad (42b)$$

The Riemann sphere corresponds to the Bloch sphere of quantum—or polaritonic—states available to a coupled-system, and it can be shown [17] that the plane can be identified as the real-physical plane where the fields are evolving. This is revealed by the motion of the core—neatly identifiable as the single point of zero density—itsself follows such an Apollonius circle. Bringing the dynamics on a sphere simplifies it considerably [37], as the Rabi oscillations for any quantum state become simply circles on the sphere (reduced to a point at the poles in the case of polaritonic eigenstates). The main axis of this sphere is here set horizontal with respect to the complex plane. Detuning between the modes has the effect of tilting the plane of the circles on the sphere. It is worth noting that also the complex polar coordinates of the sphere, thanks to the stereographic projection, are mapped into two families of mutually orthogonal Apollonian circles in the 2D real space as well. An example of this is shown in the Supplementary Movie SM4 [41]. The identification of the complex plane from the stereographic projection to the physical plane for the fields allow the interpretation of the two wavefunctions  $\psi_{C,X}$  as the breakdown of a wider and more natural object, living in a different space, to describe the dynamics. This object, the full-wavefunction (as opposed to the cavity-wavefunction or the exciton-wavefunction), provides the density of any quantum states present in the system at any time. The peculiar dynamics observed in Fig. 6 becomes a simple rigid rotation in time of the full-wavefunction on its Bloch sphere, as expected from the linear Rabi dynamics. The role of the displaced vortices (33) in this case is to prepare an initial condition that covers the entire sphere, since the vortex morphology makes it so that any quantum state is realized at any time at one, and only one, point in space. Any such point with a given quantum state undergoes simple Rabi oscillations, corresponding to, on the sphere, its rotation along its own circle.

<sup>3</sup>By definition, the dressed states provide a basis of states in which (32) is diagonal with hence no evolution in time.

At such, this establishes a homeomorphism between the Riemann sphere (Bloch sphere of quantum states) and the complex plane (real physical space) [17], that accounts very simply for the vortex core dynamics, making it only a particular case, namely, the state perpendicular to that chosen for the observation, in our case, the pure-excitonic state, since the observation is made with photons. Any other quantum state can then be seen to undergo a similar dynamics. This also explains why the core can, in this case like in previous ones, also be sent arbitrarily far including to infinity, as a result of the stereographic projection. In all cases, the motion is a smooth one at uniform speed on the sphere. If the system is prepared in such a way as to make the corresponding circle on the sphere to pass by its projection point, the corresponding trajectory will be distorted in the plane to pass by infinity. Such a case is considered in appendix B. This considerable simplification of an otherwise intricate dynamics is very appealing and calls for its generalization to the other systems. The phenomenology being so similar, one could expect that there also exist equivalent parametric or phase spaces to be defined in which the intricate dynamics of the anharmonic or squeezed cases becomes trivial and physically transparent. This remains for us, however, an open question.

## 6. SUMMARY AND CONCLUSIONS

We have shown how displaced vortices can lead to interesting dynamics of both the vortex core itself and the total angular momentum of the field, in a variety of platforms in the linear regime. Our choice of platforms included various types of confining potentials as well as coupled condensates (in the limit of low densities where interactions do not play a role). In all cases, we have highlighted the different behaviour and character of the vortex as seen through the dynamics of its core, its morphology (phase map structure) and total angular momentum. While all are intrinsically connected, they can follow entirely different types of dynamics, for instance with a complex underlying evolution of the vortex morphology, with creation of vortex-antivortex pairs, and cores displaying sequences of accelerations and decelerations with possible transit to infinity, while the net angular momentum can remain unaffected. More specifically, a displaced-vortex in a radial potential keeps its OAM constant, as expected, despite the core moving on circular or elliptic orbits with even possible secondary vortex-antivortex pair creations due to self-interferences of the wavepacket. In the presence of an asymmetry of the potential, either due to different types or even simply different magnitudes of the confinement in different directions, the OAM becomes time-varying and the field displays a striking phenomenology, notably for the vortex core that can be sent cyclically to infinity with sequences of extreme accelerations and decelerations. The phenomenology can also hold without confining potentials, as illustrated by Rabi-coupled fields where the results can be further interpreted as a topological homeomorphism linking the Bloch sphere of possible quantum states for the system with the real physical plane. The salient result across all the different cases is that of a striking motion of the vortex core with an intricate dynamical morphology of the beam, being distinct from and do not necessarily implying a time-varying OAM per particle, whereas the latter always imply some offset core and its morphology reshaping. When this is the case, the core cannot be described as a mechanical point-like object with an effective mass which otherwise allows it to account for the dynamical properties of the system, namely, its momenta (linear and angular) and energies (potential and kinetics). The



absence of interactions was chosen in the models for simplicity and to provide closed-form solutions, but numerical simulations show that the phenomenology survives in their presence. This provides opportunities for new types of micro-control and manipulations of small objects with exotic wavepackets, similarly to Airy beams interacting with light particles [42]. In our case, the time-varying angular momentum can exert a torque on the objects immersed in the fluids set in motion as shown in the text, or provide other services in precision meteorology, such as gyroscopes and even Casimir torque measurements, or to exploit the periodicity of the system for instance to realize a hybrid optomechanical torsion pendulum. Much control is available from the beam shape and morphology, that is easily tuneable with a sequence of control optical pulses, as already demonstrated experimentally. The topology of the structured light thus emitted could also be useful even in a pure linear context, offering an additional degree of freedom of possible benefit for applications of OAM signal encoding and transmission.

## DISCLOSURES

The authors declare no conflicts of interest.

## APPENDIX

### A. SIMPLIFIED COUPLED-FIELD EXPRESSIONS

It is possible to find a simpler version of the solutions given in Eqs. (38–39). Starting from the exact expression for the two coupled fields in the reciprocal space (34), and ignoring all terms with a  $k$  dependency, the dynamics remains in the real-space domain within the extent fixed by the size of the initial packet. We can then ignore diffusive effects or dispersive ones in the dynamics of the solutions. Note that real-space solutions of (36) include diffusion, which comes from the exponential term  $e^{-ik^2 M_+ t/2\hbar}$  in Eqs. (34). Without such effects, one gets the desired solutions:

$$\begin{aligned} \tilde{\psi}_C = & \left[ \cos(\omega_R t) - \frac{i\delta}{2\omega_R} \sin(\omega_R t) \right] (\tilde{\psi}_C)|_{t=0} \\ & - \frac{i\Omega}{\omega_R} \sin(\omega_R t) (\tilde{\psi}_X)|_{t=0}, \end{aligned} \quad (43a)$$

$$\begin{aligned} \tilde{\psi}_X = & - \frac{i\Omega}{\omega_R} \sin(\omega_R t) (\tilde{\psi}_C)|_{t=0} \\ & + \left[ \cos(\omega_R t) + \frac{i\delta}{2\omega_R} \sin(\omega_R t) \right] (\tilde{\psi}_X)|_{t=0}, \end{aligned} \quad (43b)$$

which, after taking their inverse Fourier transform, yield the simplified real-space form (38).

### B. VORTEX CORE MOTION ON THE RIEMANN SPHERE

We provide one example of the dynamics of the  $\mathcal{Z}$  point on the Riemann sphere, that involves infinity. We consider vortex cores in the photon and exciton fields located at, respectively,  $(-w, 0)$  and  $(0, 0)$  in real space. We assume no energy-detuning. The corresponding  $\mathcal{Z}$  points are then given as  $\mathcal{Z}_C(t) = i \tan \Omega t$  and  $\mathcal{Z}_X(t) = -i \cot \Omega t$ , which move along the imaginary axis of the complex plane (distinct from 2D real space). At  $t = 0$ ,  $\mathcal{Z}_X$  is a point at infinity, in  $t = \pi/(2\Omega)$  it reaches the origin of the complex plane and then in  $t = \pi/\Omega$  it is again sent at infinity. In contrast,  $\mathcal{Z}_C$  is initially positioned at the origin, then goes to infinity, and finally in  $t = \pi/\Omega$  it reappears at the origin. In both cases,  $\frac{d}{dt} \mathcal{Z}_{C,X}$  is not a constant and such trajectories

even involve infinite accelerations and decelerations. However, points on the Riemann sphere have a smooth, uniform-speed dynamics. Indeed, the corresponding points on the sphere are  $(0, -\sin 2\Omega t, \cos 2\Omega t)$  for  $\mathcal{Z}_C$  and  $(0, \sin 2\Omega t, -\cos 2\Omega t)$  for  $\mathcal{Z}_X$ , as is obtained directly from Eqs. (42). This is the equation for a circle on the sphere, on which the points move with a constant angular speed of  $2\Omega$ . The described situation can be realized starting from a specific initial condition of the form (33). The same picture can be extended, with different parameters but in the same form, to points in the real space, where the relevant  $\mathcal{Z}$  point moves on an associated Apollonius circle [17].

## C. CAPTIONS TO SUPPLEMENTARY MOVIES

**Movie SM1** Dynamics of an off-centered vortex in an infinite circular quantum well. Some frames of the movie are shown in Fig. 1.

**Movie SM2** Squeezing the harmonic potential in two directions leads to the weird dynamics of the vortex, that is shown in this Movie. This is for one period of the motion. Examples of the frames are shown in Fig. 5.

**Movie SM3** This displays the rotating vortex in Rabi-coupled field in the case of polariton. Here we show the photon field dynamics in one period of the motion. Some frames of photon field ( $\psi_C$ ) are shown in Fig. 6.

**Movie SM4** The movie shows the time dynamics of the photon field (intensity in black, red, yellow, white color scale) undergoing Rabi oscillations. Here a decay term has been added to illustrate how the phenomenology evolves in its presence (it produces a tilting of the sphere and its circles with respect to the plane of projection), while retaining the main features. The black circle lines represent the loci of isophase in the bare modes basis,  $\arg(X + iY) = \arg(\mathcal{Z}) = \text{constant}$ , while the white circles represent the loci of photon-exciton isocontent,  $Z = \text{constant}$ . The nodal points to the isophase circles represent the position of the vortices in the two bare modes.

## REFERENCES

1. T. D. Stanescu, *Introduction to Topological Quantum Matter and Quantum Computation* (CRC Press, New York, 2017).
2. D. Castelvecchi, "The strange topology that is reshaping physics," *Nature* **547**, 272 (2017).
3. M. R. Dennis, K. O'Holleran, and M. J. Padgett, "Singular optics: Optical vortices and polarization singularities," *Prog. Opt.* **53**, 293 (2009).
4. Y. Shen, X. Wang, Z. Xie, C. Min, X. Fu, Q. Liu, M. Gong, and X. Yuan, "Optical vortices 30 years on: OAM manipulation from topological charge to multiple singularities," *Light. Sci. & App.* **8**, 90 (2019).
5. G. Blatter, M. V. Feigel'man, V. B. Geshkenbein, A. I. Larkin, and V. M. Vinokur, "Vortices in high-temperature superconductors," *Rev. Mod. Phys.* **66**, 1125–1388 (1994).
6. A. J. Leggett, "Superfluidity," *Rev. Mod. Phys.* **71**, S318–S323 (1999).
7. M. R. Matthews, B. P. Anderson, P. C. Haljan, D. S. Hall, C. E. Wieman, and E. A. Cornell, "Vortices in a Bose-Einstein Condensate," *Phys. Rev. Lett.* **83**, 2498–2501 (1999).
8. K. G. Lagoudakis, M. Wouters, M. Richard, a. Baas, I. Carusotto, R. André, L. S. Dang, and B. Deveaud-Plédran, "Quantized vortices in an exciton polariton condensate," *Nat. Phys.* **4**, 706–710 (2008).
9. K. G. Lagoudakis, T. Ostatnický, A. V. Kavokin, Y. G. Rubo, R. André, and B. Deveaud-Plédran, "Observation of half-



- quantum vortices in an exciton-polariton condensate," *Science*. **326**, 974 (2009).
10. D. Sanvitto, F. M. Marchetti, M. H. Szymańska, G. Tosi, M. Baudisch, F. P. Laussy, D. N. Krizhanovskii, M. S. Skolnick, L. Marrucci, A. Lemaître, J. Bloch, C. Tejedor, and L. Viña, "Persistent currents and quantized vortices in a polariton superfluid," *Nat. Phys.* **6**, 527 (2010).
  11. G. Nardin, G. Grosso, Y. Léger, B. Piętko, F. Morier-Genoud, and B. Deveaud-Plédran, "Hydrodynamic nucleation of quantized vortex pairs in a polariton quantum fluid," *Nat. Phys.* **7**, 635 (2011).
  12. G. Roumpos, M. D. Fraser, A. Löffler, S. Höfling, A. Forchel, and Y. Yamamoto, "Single vortex-antivortex pair in an exciton-polariton condensate," *Nat. Phys.* **7**, 129 (2011).
  13. L. Dominici, G. Dagvadorj, J. M. Fellows, D. Ballarini, M. D. Giorgi, F. M. Marchetti, B. Piccirillo, L. Marrucci, A. Bramati, G. Gigli, M. H. Szymańska, and D. Sanvitto, "Vortex and half-vortex dynamics in a nonlinear spinor quantum fluid," *Sci. Adv.* **1**, e1500807 (2015).
  14. L. Dominici, R. Carretero-González, A. Gianfrate, J. Cuevas-Maraver, A. S. Rodrigues, D. J. Frantzeskakis, G. Lerario, D. Ballarini, M. D. Giorgi, G. Gigli, P. G. Kevrekidis, and D. Sanvitto, "Interactions and scattering of quantum vortices in a polariton fluid," *Nat. Comm.* **9**, 1467 (2018).
  15. A. M. Yao and M. J. Padgett, "Orbital angular momentum: origins, behavior and applications," *Adv. Opt. Photonics* **3**, 161 (2011).
  16. F. S. Roux, "Distribution of angular momentum and vortex morphology in optical beams," *Opt. Commun.* **242**, 45 – 55 (2004).
  17. L. Dominici, N. Voronova, D. Colas, A. Gianfrate, A. Rahmani, D. Ballarini, M. De Giorgi, G. Gigli, F. P. Laussy, and D. Sanvitto, "Realisation of full-Bloch beams with ultrafast Rabi-rotating vortices," preprint at <https://arxiv.org/abs/1801.02580> (2018).
  18. L. Rego, K. M. Dorney, N. J. Brooks, Q. L. Nguyen, C.-T. Liao, J. San Román, D. E. Couch, A. Liu, E. Pisanty, M. Lewenstein, L. Plaja, H. C. Kapteyn, M. M. Murnane, and C. Hernández-García, "Generation of extreme-ultraviolet beams with time-varying orbital angular momentum," *Science* **364** (2019).
  19. A. Kavokin, J. Baumberg, G. G. Malpuech, and L. F. P., *Microcavities* (Oxford University Press, Oxford, 2017), 2nd ed.
  20. A. S. Abdalla, B. Zou, Y. Ren, T. Liu, and Y. Zhang, "Generation of optical vortices by exciton polaritons in pillar semiconductor microcavities," *Opt. Express* **26**, 22273–22283 (2018).
  21. V. A. Lukoshkin, V. K. Kalevich, M. M. Afanasiev, K. V. Kavokin, Z. Hatzopoulos, P. G. Savvidis, E. S. Sedov, and A. V. Kavokin, "Persistent circular currents of exciton-polaritons in cylindrical pillar microcavities," *Phys. Rev. B* **97**, 195149 (2018).
  22. E. S. Sedov and V. A. Lukoshkin and V. K. Klaevich and P. G. Hatzopoulos and P. G. Savvidis and A. V. Kavokin, "Superfluid currents in half-moon polariton condensates," preprint at <https://arxiv.org/abs/1910.00344> (2018).
  23. "This is the link to Supplementary Movie SM1," <https://www.dropbox.com/s/f15h7hlog3zfp47/MovieSM1avi?dl=0>.
  24. S. Maji, P. Jacob, and M. M. Brundavanam, "Geometric phase and intensity-controlled extrinsic orbital angular momentum of off-axis vortex beams," *Phys. Rev. Appl.* **12**, 054053 (2019).
  25. R. Navarro, R. Carretero-González, P. J. Torres, P. G. Kevrekidis, D. J. Frantzeskakis, M. W. Ray, E. Altıntaş, and D. S. Hall, "Dynamics of a few corotating vortices in bose-einstein condensates," *Phys. Rev. Lett.* **110**, 225301 (2013).
  26. P. G. Kevrekidis, W. Wang, R. Carretero-González, D. J. Frantzeskakis, and S. Xie, "Vortex precession dynamics in general radially symmetric potential traps in two-dimensional atomic bose-einstein condensates," *Phys. Rev. A* **96**, 043612 (2017).
  27. F. Barkhausen, S. Schumacher, and X. Ma, "Multistable circular currents of polariton condensates trapped in ring potentials," *Opt. Lett.* **45**, 1192–1195 (2020).
  28. Y. V. Kartashov and D. A. Zezyulin, "Rotating patterns in polariton condensates in ring-shaped potentials under a bichromatic pump," *Opt. Lett.* **44**, 4805–4808 (2019).
  29. M. Correggi, F. Pinsker, N. Rougerie, and J. Yngvason, "Rotating superfluids in anharmonic traps: From vortex lattices to giant vortices," *Phys. Rev. A* **84**, 053614 (2011).
  30. G. Molina-Terriza, J. Recolons, J. P. Torres, L. Torner, and E. M. Wright, "Observation of the dynamical inversion of the topological charge of an optical vortex," *Phys. Rev. Lett.* **87**, 023902 (2001).
  31. Y. Zhang, X. Yang, and J. Gao, "Orbital angular momentum transformation of optical vortex with aluminum metasurfaces," *Sci. Rep.* **9**, 9133 (2019).
  32. "This is the link to Supplementary Movie SM2," <https://www.dropbox.com/s/0xhy062u607va0m/MovieSM2avi?dl=0>.
  33. A. L. Fetter, "Vortex dynamics in spin-orbit-coupled bose-einstein condensates," *Phys. Rev. A* **89**, 023629 (2014).
  34. A. Rahmani and M. Sadeghzadeh, "Polaritonic linear dynamics in Keldysh formalism," *Superlattices Microstruct.* **100**, 842 – 856 (2016).
  35. A. Rahmani and L. Dominici, "Detuning control of Rabi vortex oscillations in light-matter coupling," *Phys. Rev. B* **100**, 094310 (2019).
  36. N. S. Voronova, A. A. Elistratov, and Y. E. Lozovik, "Detuning-controlled internal oscillations in an exciton-polariton condensate," *Phys. Rev. Lett.* **115**, 186402 (2015).
  37. A. Rahmani and F. P. Laussy, "Polaritonic Rabi and Josephson oscillations," *Sci. Reports* **6**, 28930 (2016).
  38. "This is the link to Supplementary Movie SM3," <https://www.dropbox.com/s/99g9jxwpm4bhvz/MovieSM3avi?dl=0>.
  39. D. Colas and F. P. Laussy, "Self-Interfering Wave Packets," *Phys. Rev. Lett.* **116**, 026401 (2016).
  40. T. Needham, *Visual Complex Analysis* (Oxford University Press, New York, 1997).
  41. "This is the link to Supplementary Movie SM3," <https://www.dropbox.com/s/qiuxtsbj750q5uq/MovieSM4mp4?dl=0>.
  42. J. Baumgartl, M. Mazilu, and K. Dholakia, "Optically mediated particle clearing using Airy wavepackets," *Nat. Photon.* **2**, 675 (2008).